(2)

TECHNICAL REPORT BRL-TR-3150

BRL

THREE DIMENSIONAL FLOW CALCULATIONS FOR A PROJECTILE WITH STANDARD AND DOME BASES

JUBARAJ SAHU
CHARLES J. NIETUBICZ

SEPTEMBER 1990

U.S. ARMY LABORATORY COMMAND

BALLISTIC RESEARCH LABORATORY
ABERDEEN PROVING GROUND, MARYLAND

NOTICES

Destroy this report when it is no longer needed. DO NOT return it to the originator.

Additional copies of this report may be obtained from the National Technical Information Service, U.S. Department of Commerce, 5285 Port Royal Road, Springfield, VA 22161.

The findings of this report are not to be construed as an official Department of the Army position, unless so designated by other authorized documents.

The use of trade names or manufacturers' names in this report does not constitute indorsement of any commercial product.

REPORT DOCUMENTATION PAGE

Form Approved
OMB No. 0704-0188

1. AGENCY USE ONLY (Leave blank)	2. REPORT DATE	3. REPORT TYPE AND DATES COVERED
	September 1990	Final, Jan 89 - Jul 90

4. TITLE AND SUBTITLE

THREE DIMENSIONAL FLOW CALCULATIONS FOR A PROJECTILE WITH STANDARD AND DOME BASES

5. FUNDING NUMBERS

1L162618AH80
62618A-00-001 AJ

6. AUTHOR(S)

JUBARAJ SAHU and CHARLES J. NIETUBICZ

7. PERFORMING ORGANIZATION NAME(S) AND ADDRESS(ES)

8. PERFORMING ORGANIZATION REPORT NUMBER

9. SPONSORING/MONITORING AGENCY NAME(S) AND ADDRESS(ES)

Ballistic Research Laboratory
ATTN: SLCBR-DD-T
Aberdeen Proving Ground, MD 21005-5066

10. SPONSORING/MONITORING AGENCY REPORT NUMBER

BRL-TR-3150

11. SUPPLEMENTARY NOTES

12a. DISTRIBUTION/AVAILABILITY STATEMENT

Approved for public release; distribution is unlimited

12b. DISTRIBUTION CODE

13. ABSTRACT (Maximum 200 words)

Test firings of the 155mm XM825 artillery projectile have shown that its flight performance was affected by configurational changes to the base cavity. This was an unexpected result, and a clear understanding of why these changes affected the flight behavior did not exist. A computational study has been made for the two different base cavity configurations which were flight tested. Flow field computations have been performed at 0.8 < M < 1.5 and alpha = 4.0 degrees using a recently developed 3D Navier-Stokes code. The computed results show the qualitative features of the base region flow field for the two base cavities. The base changes are found to alter the recirculation patterns in the wake which in turn affect the expansion at the base corner. These changes in the flow structure contribute to small changes in the base pressure. Aerodynamic force and moment coefficients have been obtained from the computed pressures and are presented as a function of Mach number. Computed results show small differences in normal force and pitching moment coefficients similar to that found in the range data. Keywords:

14. SUBJECT TERMS			15. NUMBER OF PAGES
Numerical Computations, Transonic, Angle of Attack, Base Cavities, Yaw, Force and Moment Coefficients			30
			16. PRICE CODE
17. SECURITY CLASSIFICATION OF REPORT	18. SECURITY CLASSIFICATION OF THIS PAGE	19. SECURITY CLASSIFICATION OF ABSTRACT	20. LIMITATION OF ABSTRACT
UNCLASSIFIED	UNCLASSIFIED	UNCLASSIFIED	UL

NSN 7540-01-280-5500

Standard Form 298 (Rev 2-89)
Prescribed by ANSI Std 239-18
298-102

INTENTIONALLY LEFT BLANK.

TABLE OF CONTENTS

Page

I. INTRODUCTION 1

II. GOVERNING EQUATIONS AND SOLUTION TECHNIQUE 2

1. GOVERNING EQUATIONS 2

2. NUMERICAL TECHNIQUE 4

3. COMPOSITE GRID SCHEME 5

III. MODEL GEOMETRY AND COMPUTATIONAL GRID 6

IV. RESULTS 6

V. CONCLUSIONS 8

REFERENCES 21

LIST OF SYMBOLS 23

DISTRIBUTION LIST 25

INTENTIONALLY LEFT BLANK.

LIST OF FIGURES

Figure		Page
1	Actual XM825 projectile.	9
2	Computational model.	10
3	Base cavity configurations.	11
4	Computational grid for the standard base.	12
5	Computational grid for the dome base.	12
6	Base region grid for the standard base.	13
7	Base region grid for the dome base.	13
8	Velocity vectors in the base region, M_∞=0.98, $\alpha = 0.0^0$, (standard base).	14
9	Velocity vectors in the base region, M_∞=0.98, $\alpha = 0.0^0$, (dome base).	14
10	Velocity vectors in the base region, M_∞=0.98, $\alpha = 4.0^0$, (standard base).	15
11	Velocity vectors in the base region, M_∞=0.98, $\alpha = 4.0^0$, (dome base).	15
12	Mach number contours, M_∞=0.98, $\alpha = 0.0^0$, (standard base).	16
13	Mach number contours, M_∞=0.98, $\alpha = 0.0^0$, (dome base).	16
14	Mach number contours, M_∞=0.98, $\alpha = 4.0^0$, (standard base).	17
15	Mach number contours, M_∞=0.98, $\alpha = 4.0^0$, (dome base).	17
16	Base pressure distribution for the dome base, M_∞=1.1, $\alpha = 4.0^0$.	18
17	Normal force coefficient, C_N vs Mach number (dome base).	19
18	Normal force coefficient, C_N vs Mach number (standard base and dome base).	19
19	Pitching moment coefficient, C_{m_o} vs Mach number (standard base and dome base).	20

INTENTIONALLY LEFT BLANK.

I. INTRODUCTION

The ability to compute the base region flow field for projectile configurations using Navier-Stokes computational techniques has been developed over the past few years[1,2,3] This capability is very important for determining aerodynamic coefficient data including the total aerodynamic drag. The majority of base flow calculations to date have modeled the base region as a flat solid surface. Many of the actual configurations have some form of base cavity. General opinion has been that the inclusion of a base cavity or modifications to the interior cavity of a projectile base would have little or no effect on the overall flight performance parameters.

The M825 projectile under certain conditions is expected to be acroballistically similar to its parent configuration the M483A1. The M825 has an aluminum/steel base which is configured as a flat cavity (standard). A recent Product Improvement Program (PIP), undertaken to reduce the production costs and improve shell integrity, resulted in the design of a new base configuration. This new PIP configuration has an all steel base and contains a dome cavity. A series of aeroballistic tests [4] were conducted in the Transonic Range Facility of the US Army Ballistic Research Laboratory (BRL), to determine any difference in the aeroballistics which may occur between the standard and dome base configurations. As a result of these tests, differences in aerodynamic performance were found to exist between the two rounds. The most significant changes in the aerodynamic data were in the lift and static moment coefficients. The drag was found to differ by a few percent with the dome configuration having the lower drag at low transonic speeds.

A computational study was undertaken to determine the ability of the present Navier-Stokes codes to predict these differences and to further understand the fluid dynamic behavior which can account for such small changes. The use of Navier-Stokes codes can provide a detailed description of the flow field associated with the M825 configuration as well as the integrated aerodynamic coefficients. The initial results for the zero degree angle of attack case have been reported by Sahu et. al.[5] . This was accomplished using an axisymmetric base flow code and the results showed the same effect as the range data, that is, a small reduction in the total aerodynamic drag at low transonic speeds ($M < 0.95$) for the dome base configuration. The trend reversed at high transonic speeds ($M > 0.98$). This report describes an extension of that work into three dimensions.

Numerical computations have been performed using a 3D zonal, implicit Navier-Stokes code. The Mach number range was $0.8 < M < 1.5$ for an angle of attack, $\alpha = 4.0^0$. Results presented include the qualitative features of the base region flow field for the two base cavities. Aerodynamic force and moment coefficients have been obtained from the computed solutions and are presented as a function of Mach number. Computed results show small differences in normal force and pitching moment coefficients similar to that found in the range data.

II. GOVERNING EQUATIONS AND SOLUTION TECHNIQUE

The complete set of time-dependent thin-layer Navier-Stokes equations is solved numerically to obtain a solution to this problem. The numerical technique used is an implicit finite difference scheme. Although time-dependent calculations are made, the transient flow is not of primary interest at the present time. The steady flow, which is the desired result, is obtained in a time asymptotic fashion.

1. GOVERNING EQUATIONS

The complete set of three dimensional, time dependent, generalized geometry, thin-layer, Navier-Stokes equations for general spatial coordinates ξ, η, ζ can be written as[6]:

$$\partial_\tau \hat{q} + \partial_\xi \hat{F} + \partial_\eta \hat{G} + \partial_\zeta \hat{H} = Re^{-1} \partial_\zeta \hat{S} \tag{1}$$

where

$$\begin{aligned} \xi &= \xi(x, y, z, t) && \text{- longitudinal coordinate} \\ \eta &= \eta(x, y, z, t) && \text{- circumferential coordinate} \\ \zeta &= \zeta(x, y, z, t) && \text{- nearly normal coordinate} \\ \tau &= t && \text{- time} \end{aligned}$$

and

$$\hat{q} = \frac{1}{J} \begin{bmatrix} \rho \\ \rho u \\ \rho v \\ \rho w \\ e \end{bmatrix} \qquad \hat{F} = \frac{1}{J} \begin{bmatrix} \rho U \\ \rho u U + \xi_x p \\ \rho v U + \xi_y p \\ \rho w U + \xi_z p \\ (e+p)U - \xi_t p \end{bmatrix}$$

$$\hat{G} = \frac{1}{J} \begin{bmatrix} \rho V \\ \rho u V + \eta_x p \\ \rho v V + \eta_y p \\ \rho w V + \eta_z p \\ (e+p)V - \eta_t p \end{bmatrix} \qquad \hat{H} = \frac{1}{J} \begin{bmatrix} \rho W \\ \rho u W + \zeta_x p \\ \rho v W + \zeta_y p \\ \rho w W + \zeta_z p \\ (e+p)W - \zeta_t p \end{bmatrix} \tag{2}$$

and where

$$\hat{S} = \frac{1}{J}\begin{bmatrix} 0 \\ \mu(\zeta_x^2+\zeta_y^2+\zeta_z^2)u_\zeta + \frac{\mu}{3}(\zeta_x u_\zeta + \zeta_y v_\zeta + \zeta_z w_\zeta)\zeta_x \\ \mu(\zeta_x^2+\zeta_y^2+\zeta_z^2)v_\zeta + \frac{\mu}{3}(\zeta_x u_\zeta + \zeta_y v_\zeta + \zeta_z w_\zeta)\zeta_y \\ \mu(\zeta_x^2+\zeta_y^2+\zeta_z^2)w_\zeta + \frac{\mu}{3}(\zeta_x u_\zeta + \zeta_y v_\zeta + \zeta_z w_\zeta)\zeta_z \\ \{(\zeta_x^2+\zeta_y^2+\zeta_z^2)[\frac{\mu}{2}(u^2+v^2+w^2)_\zeta \\ + \frac{\kappa a_\zeta^2}{Pr\,(\gamma-1)}] \\ + \frac{\mu}{3}(\zeta_x u + \zeta_y v + \zeta_z w)(\zeta_x u_\zeta + \zeta_y v_\zeta + \zeta_z w_\zeta)\} \end{bmatrix} \tag{3}$$

In equation (1), the thin-layer approximation is used and the viscous terms involving velocity gradients in both the longitudinal and circumferential directions are neglected. The viscous terms are retained, however, for velocity gradients in a direction nearly normal to the surface where large flowfield gradients exist. These viscous terms in ζ are collected into the vector $\hat{S}$.

For this computation, the diffusion coefficients μ and κ contain molecular and turbulent parts. The turbulent contributions are supplied through an algebraic eddy-viscosity hypothesis which has been developed by Baldwin and Lomax.[7]

The velocities in the ξ, η, and ζ coordinate directions can be written

$$\begin{aligned} U &= \xi_t + u\xi_x + v\xi_y + w\xi_z \\ V &= \eta_t + u\eta_x + v\eta_y + w\eta_z \\ W &= \zeta_t + u\zeta_x + v\zeta_y + w\zeta_z \end{aligned}$$

which represent the contravariant velocity components.

The Cartesian velocity components (u, v, w) are retained as the dependent variables and are nondimensionalized with respect to a_∞ (the free stream speed of sound). The local pressure is determined using the relation

$$p = (\gamma-1)[e - 0.5\rho(u^2+v^2+w^2)] \tag{4}$$

where γ is the ratio of specific heats. Density (ρ) is referenced to ρ_∞ and the total energy (e) to $\rho_\infty a_\infty^2$. The transport coefficients are also nondimensionalized with respect to the corresponding free stream variables. Thus the Prandtl number which appears in $\hat{S}$ is defined as $Pr = c_{p\infty}\mu_\infty/\kappa_\infty$.

In differencing these equations it is often advantageous to difference about a known base solution denoted by subscript $_0$ as

$$\delta_\tau(\hat{Q}-\hat{Q}_0) \quad +\delta_\xi(\hat{F}-\hat{F}_0)+\delta_\eta(\hat{G}-\hat{G}_0)+\delta_\zeta(\hat{H}-\hat{H}_0)-Re^{-1}\delta_\zeta(\hat{S}-\hat{S}_0) \qquad (5)$$
$$= -\partial_\tau\hat{Q}_0-\partial_\xi\hat{F}_0-\partial_\eta\hat{G}_0-\partial_\zeta\hat{H}_0+Re^{-1}\partial_\zeta\hat{S}_0$$

where δ indicates a general difference operator, and ∂ is the differential operator. If the base state can be properly chosen, the differenced quantities can have smaller and smoother variation and therefore less differencing error.

2. NUMERICAL TECHNIQUE

The implicit approximately factored scheme for the thin layer Navier Stokes equations that uses central differencing in the η and ζ directions and upwinding in ξ is written in the form

$$\begin{aligned}
&\left[I+h\delta_\xi^b(\hat{A}^+)^r+h\delta_\zeta\hat{C}^n-hRe^{-1}\bar{\delta}_\zeta J^{-1}\hat{M}^nJ-D_i|_\zeta\right] \\
&\qquad\times\left[I+h\delta_\xi^f(\hat{A}^-)^n+h\delta_\eta\hat{B}^n-D_i|_\eta\right]\Delta\hat{Q}^n= \\
&-\Delta t\{\delta_\xi^b[(\hat{F}^+)^n-\hat{F}_\infty^+]+\delta_\xi^f[(\hat{F}^-)^n-\hat{F}_\infty^-]+\delta_\eta(\hat{G}^n-\hat{G}_\infty) \\
&+\delta_\zeta(\hat{H}^n-\hat{H}_\infty)-Re^{-1}\bar{\delta}_\zeta(\hat{S}^n-\hat{S}_\infty)\}-D_e(\hat{Q}^n-\hat{Q}_\infty)
\end{aligned} \qquad (6)$$

where $h=\Delta t$ or $(\Delta t)/2$ and the free stream base solution is used. Here δ is typically a three point second order accurate central difference operator, $\bar{\delta}$ is a midpoint operator used with the viscous terms, and the operators δ_ξ^b and δ_ξ^f are backward and forward three-point difference operators. The flux $\hat{F}$ has been eigensplit and the matrices $\hat{A},\hat{B},\hat{C}$, and $\hat{M}$ result from local linearization of the fluxes about the previous time level. Here J denotes the Jacobian of the coordinate transformation. Dissipation operators, D_e and D_i are used in the central space differencing directions.

The smoothing terms used in the present study are of the form:

$$D_e|_\eta=(\Delta t)J^{-1}[\epsilon_2\bar{\delta}\rho(B)\beta\bar{\delta}+\epsilon_4\bar{\delta}\frac{\rho(B)}{1+\beta}\bar{\delta}^3]|_\eta J$$

$$D_i|_\eta=(\Delta t)J^{-1}[\epsilon_2\bar{\delta}\rho(B)\beta\bar{\delta}+2.5\epsilon_4\bar{\delta}\rho(B)\bar{\delta}]J$$

where $\beta=\frac{|\delta^2 p|}{|(1+\delta^2)p|}$ and where $\rho(B)$ is the true spectral radius of B. The idea here is that the fourth difference will be tuned down near shocks, that is, as β gets large the weight on the fourth difference drops down while the second difference tunes up.

For simplicity, all the boundary conditions have been imposed explicitly. On the body surface, the no-slip boundary condition is used and the wall temperature is specified. Free stream boundary conditions are used at the computational outer boundary. A symmetry

boundary condition is imposed at the circumferential edges of the grid while a simple extrapolation is used at the downstream boundary. The flowfield is initially set to free stream conditions everywhere and then advanced in time until a steady state solution is obtained. Atmospheric flight conditions were used.

3. COMPOSITE GRID SCHEME

In the present work, a simple composite grid scheme[8] has been used where a large single grid is split into a number of smaller grids so that computations can be performed on each of these grids separately. These grids use the available core memory one grid at a time, while the remaining grids are stored on an external disk storage device such as the solid state disk device (SSD) of the Cray X-MP/48 computer. The Cray-2 has a large incore memory to fit the large single grid. However, for accurate geometric modeling of complex projectile configurations which include blunt noses, sharp corners and base cavities, it is also desirable to split the large data base into a few smaller zones on Cray-2 as well.

The use of a composite grid scheme requires special care in storing and fetching the interface boundary data , i.e., the communication between the various zones. In the present scheme, there is a one to one mapping of the grid points at the interface boundaries and thus, no interpolations are required. Details of the data storage, data transfer and other pertinent information such as metric and differencing accuracy at the interfaces can be found in Reference 8 and 9. This scheme has been successfully used by Sahu[9] to compute three dimensional transonic flow over two projectiles . The computed results clearly showed the transonic critical aerodynamic behavior in pitching moment coefficient observed in free flights. The present work is a further application of this technique to a more complicated projectile with base cavities.

III. MODEL GEOMETRY AND COMPUTATIONAL GRID

The external configuration of the M825, excluding the base, is similar to the M483A1 shown in Figure 1. The features of this projectile which have not been modeled exactly are the meplat on the fuze and the rotating band near the base. The rotating band was eliminated for simplicity and the meplat was modeled as a hemisphere cap. The computational model is shown in Figure 2 and consists of a 2.84 caliber nose, a 2.7 caliber cylindrical section, and a 0.26 caliber 8^0 boattail. The ogive contour as well as the undercut on the cylindrical section were matched.

The current problem of interest is the effect of the different base geometries on the overall projectile aerodynamics. Figure 3 shows the standard and dome base configurations. The standard base is a combination of aluminum and steel and contains a base cavity which is characterized as a flat surface. The PIP configuration is an all steel base and is characterized as a dome surface. The cavity volume is also significantly larger for the dome configuration.

The solution technique requires the discretization of the entire flow region of interest into a suitable computational grid. The grid outer boundary has been placed at 2.5 body lengths upstream and surrounding the projectile. The downstream boundary was placed at 2 body lengths. Since the calculations are in the subsonic/transonic regime the computational boundaries must extend out beyond the influence of the body. This ensures that the boundary conditions specified in the flow code are satisfied.

Figure 4 and Figure 5 show the grids generated for the standard base and dome base configurations, respectively. Each of these grids consists of 225 points in the streamwise direction and 50 points in the normal direction. This is broken down into two sections: a body region and a base region. The surface points for each region are selected using an interactive design program. Each grid section is then computed separately using a hyperbolic grid generation program [10]. Longitudinally, there are 106 points along the projectile surface and 60 points in the base region downstream of the base corner. The normal distribution of points in base region consists of 50 points along the base cavity. An expanded three dimensional view of the base grid is shown in Figure 6. This grid has 33 points in the circumferential direction. The generally flat sections on the standard base enabled a grid to be routinely generated. However, due to the extreme concavity the grid for the dome base (Figure 7) required an increase in the smoothing values used by the hyperbolic grid generator, as well as the addition of a grid averaging technique.

IV. RESULTS

Numerical computations have been made for both the standard and the dome base configurations for a range of Mach numbers from M = 0.80 to 1.5 and at 4 degrees angle of attack. Computed results obtained at zero degree angle of attack are also included for comparison purposes.

A few qualitative results are presented next. Figure 8 and Figure 9 show the velocity

vectors in the base region for both base configurations at M_∞=0.98 and $\alpha = 0.0^0$. The recirculatory flow in the base region is evident and as expected, is symmetric. As shown in Figure 8, the recirculation region for the standard base extends to about one and a half caliber downstream of the base corner. The back flow, upon reaching the cavity follows the contour of the cavity and leaves the cavity pushing the flow upwards. The shear layer leaving the base corner is displaced upwards weakening the expansion at the base. Figure 9 for the dome configuration shows a weak secondary bubble inside the cavity in addition to the primary bubble. The flow again follows the contour of the cavity and, upon leaving the dome cavity, is almost parallel to the streamwise direction. This flow, thus, has less effect on the free shear layer and doesn't weaken the expansion at the base corner as much compared to the standard base. The net effect is that the size of the primary bubble for the dome base is slightly smaller than that for the standard base. The reattachment point is therefore closer to the base and results in lower base pressure or higher base drag at this Mach number[5] . Figure 10 and Figure 11 show the velocity vectors in the base region for the base configurations at M_∞=0.98 and $\alpha = 4.0^0$ for both windside (bottom half) and leeside (top half). Again the recirculatory flow in the base region is evident and as expected, the flow in the wake is asymmetric. As shown in these figures, the separation bubbles on windside and leeside in the wake differ in size and shape (the one on windside being more thin and elongated). In addition, a number of secondary separation bubbles can be seen to form inside the cavity for both base configurations. These changes in the flow structure contribute to small changes in the base pressure and thus, to the aerodynamic forces and moments.

Figure 12 and Figure 13 show the Mach number contours in the base region for both base configurations at M_∞=0.98 and $\alpha = 0.0^0$. These figures show the flow expansion at the ogive corner, boattail corner and the base corner. One can also see a shock wave on the cylinder portion of the projectile as well as a recompression shock system which exists downstream of the base corner. The flow field is symmetric for this condition. As angle of attack is increased to 4 degrees, the flow field becomes asymmetric (see Figure 14 and Figure 15). A small asymmetry can be observed in the location of the shock wave on the cylinder. The windside shock is further aft compared to the corresponding one on the leeside. The asymmetry can be clearly seen in the wake flow and its associated shock system. As can be seen in these figures, the wake flow field changes for the different base configurations.

The entire flowfield over the projectile including the base region is computed. Therefore, the computed results include any upstream influence the base region flow may have on the boattail flowfield. Surface pressures including the base pressure and the viscous stresses are known from the computed flow field and can be integrated to give the aerodynamic forces and moments. Figure 16 shows the computed base pressure distribution for the dome base configuration at M_∞=1.1 and $\alpha = 4.0^0$ for windside and leeside. As seen in this figure, the pressure on the windside (Z/D=-0.5) is higher than the pressure on leeside. Since this pressure acts normal to the inside surface of the cavity, it produces a downward force (see Figure 17). Figure 17 shows the normal force coefficient for the dome base as a function of Mach number. The dotted line represents the normal force coefficient, C_N for the dome base projectile where the base region is excluded in the force and moment calculations. The solid line is for the entire projectile including the contribution from the

base region. As mentioned earlier, the base region produces a negative contribution and thus, the normal force is reduced somewhat for high transonic speeds ($M > 0.90$). The reverse is true for low transonic speeds ($M < 0.85$) . Figure 18 shows the normal force coefficient comparison for both base configurations as a function of Mach number. The dotted line represents the dome base result whereas the solid line shows the result for the standard base. As seen in this figure, the dome base has a higher normal force coefficient at transonic speeds compared to the standard base. The difference is small, of the order of a few percent, at higher transonic speeds ($M > 0.90$) and gets as large as 10-12 % at low transonic speeds ($M < 0.90$).

An aerodynamic coefficient which is of primary concern is the pitching moment coefficient, C_{m_α}. Figure 19 shows the C_{m_α} comparison for both base configurations. The computed C_{m_α} is also compared with the range data [4] for both base configurations. Here C_{m_α} is referenced to the center of gravity of the projectile. The computed result clearly shows a sharp rise in C_{m_α} between M = 0.80 to 0.88 which is followed by a sharp drop as Mach number is increased to M = 0.95 . As the Mach number is increased further C_{m_α} rises gradually again which is unlike the behavior of other projectiles such as the M549 projectile [9]. This critical behavior in C_{m_α} observed in the data is clearly predicted in the numerical computations. The overall comparison of the computed result with the range data is fair. As seen in the range data, the dome base configuration has lower C_{m_α} at transonic speeds compared to the standard base configuration and this trend is also seen in the computed results.

V. CONCLUSIONS

Three dimensional numerical computations have been made for a projectile with two base cavity configurations at transonic speeds. Computed results show differences in the qualitative features of the base region flowfield between the two base cavities. Changes in the base cavity configuration have been found to affect the normal force and pitching moment coefficient. Differences in these coefficients of between 0 to 12% have been predicted and are compared with the range data. The dome base configuration produces a higher normal force and a lower pitching moment than the standard base at these transonic speeds and shows the same trend observed in the range data.

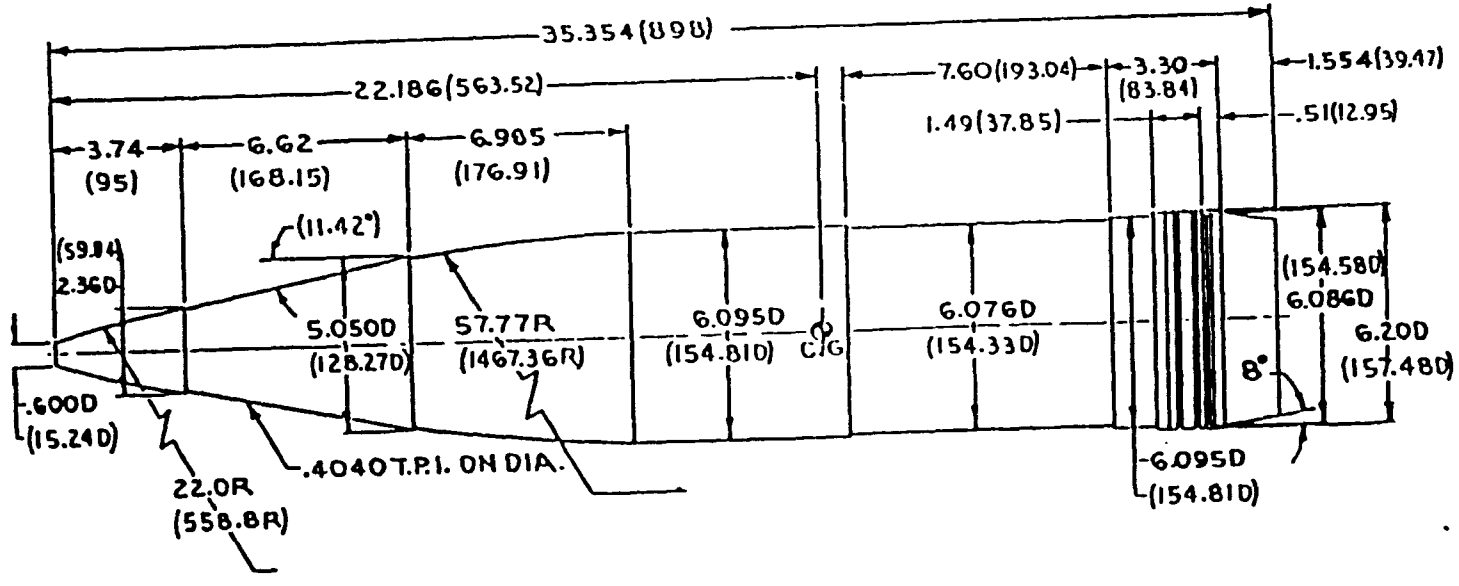

NOTE:-DIMS. ARE IN INCHES & MM.( )

Figure 1: Actual XM825 projectile.

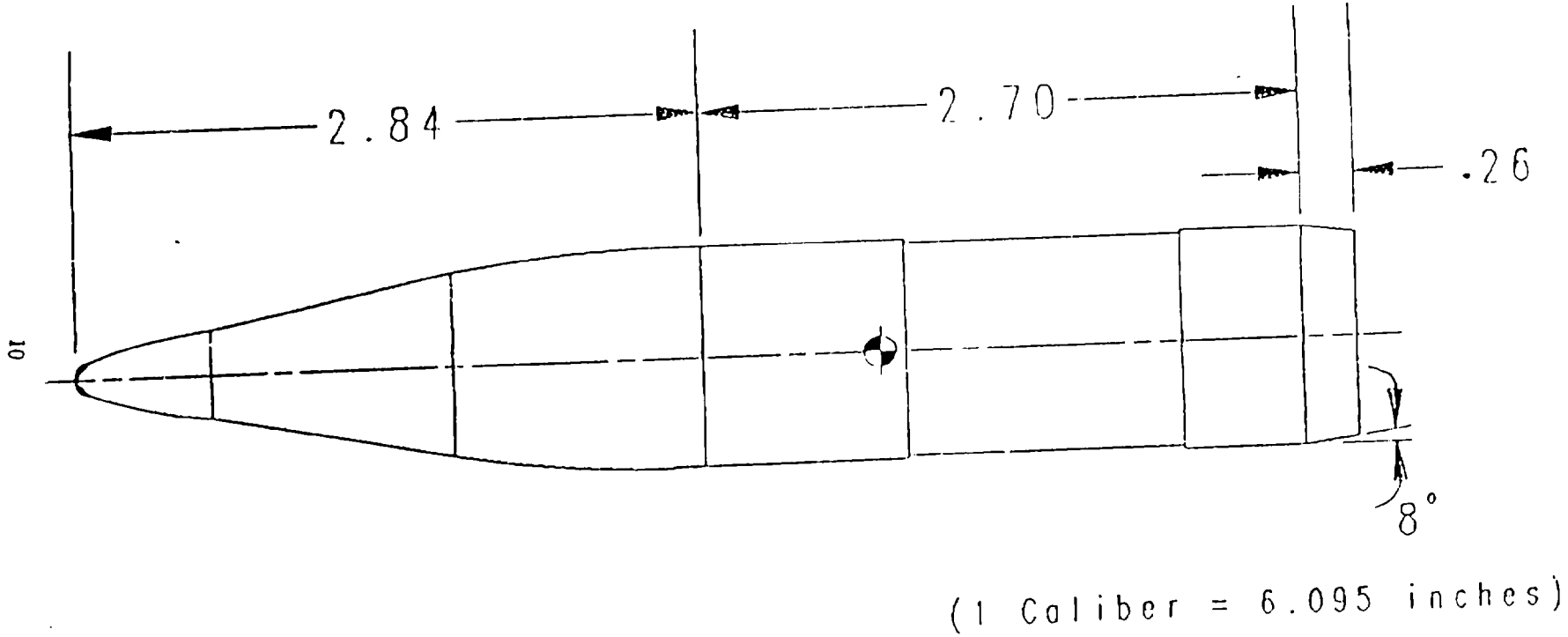

Figure 2: Computational model.

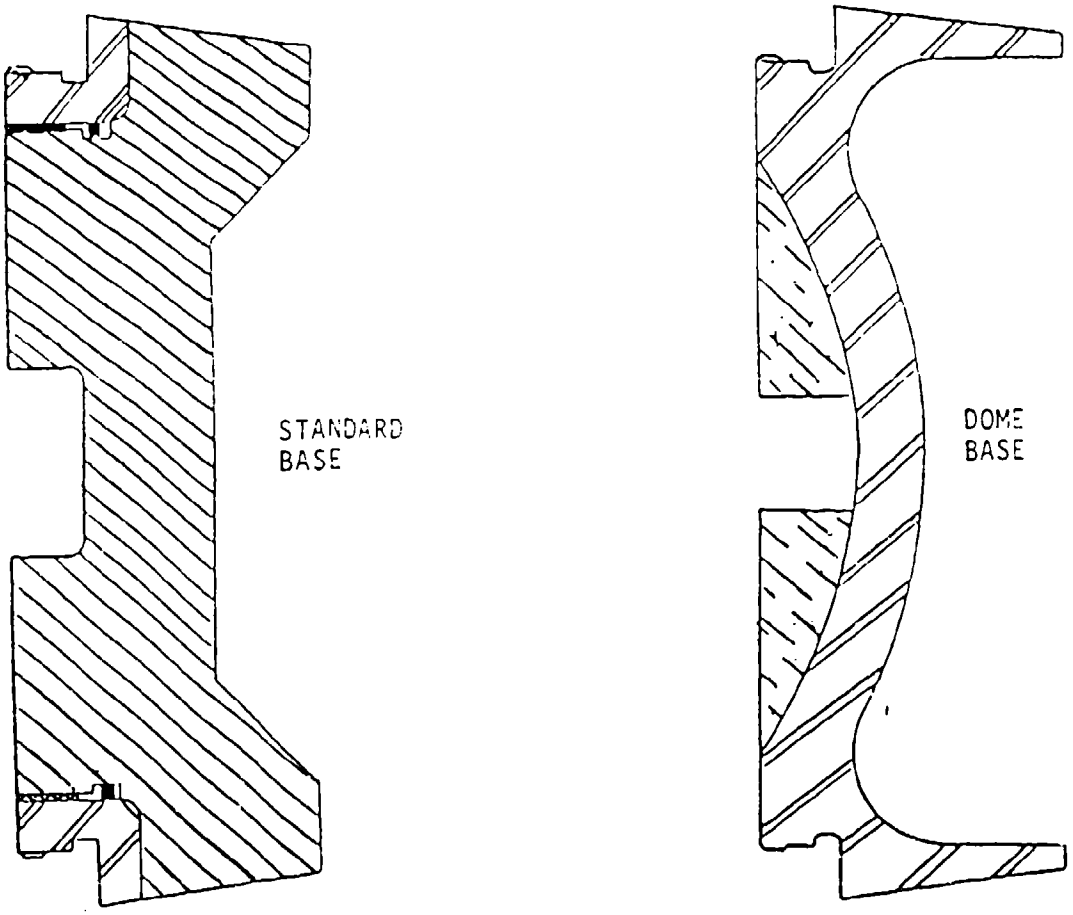

Figure 3: Base cavity configurations.

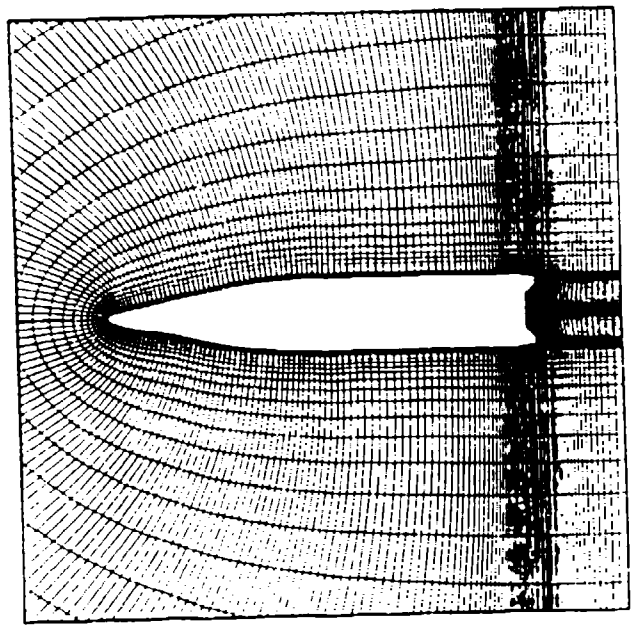

Figure 4: Computational grid for the standard base.

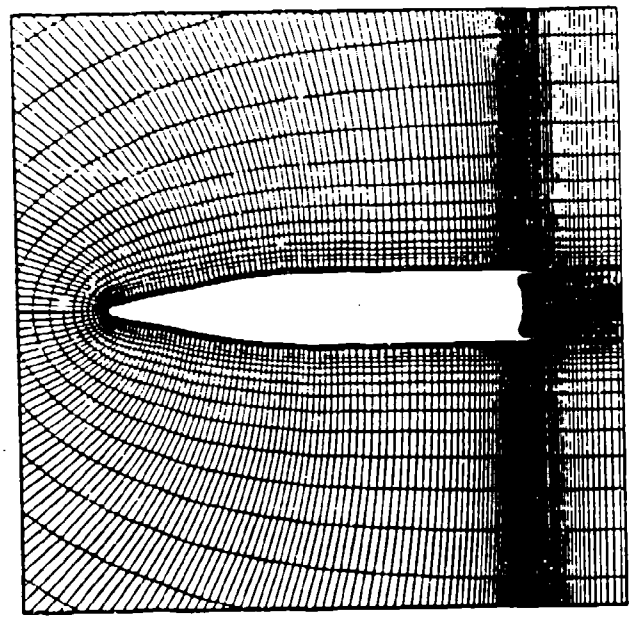

Figure 5: Computational grid for the dome base.

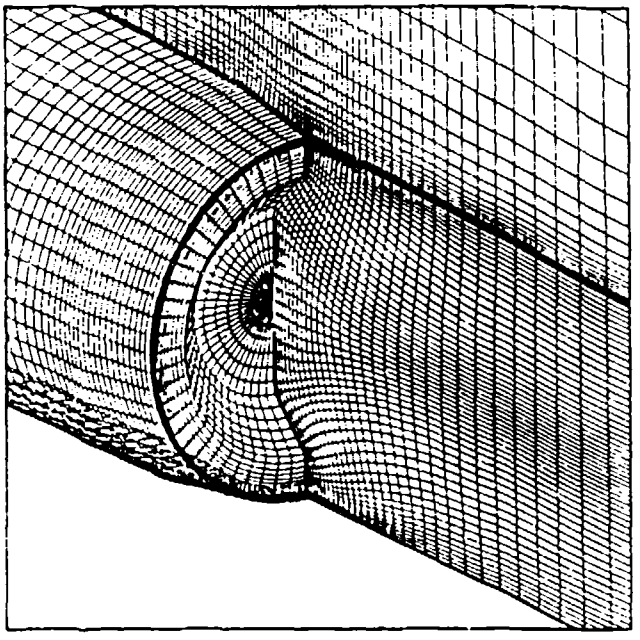

Figure 6. Base region grid for the standard base.

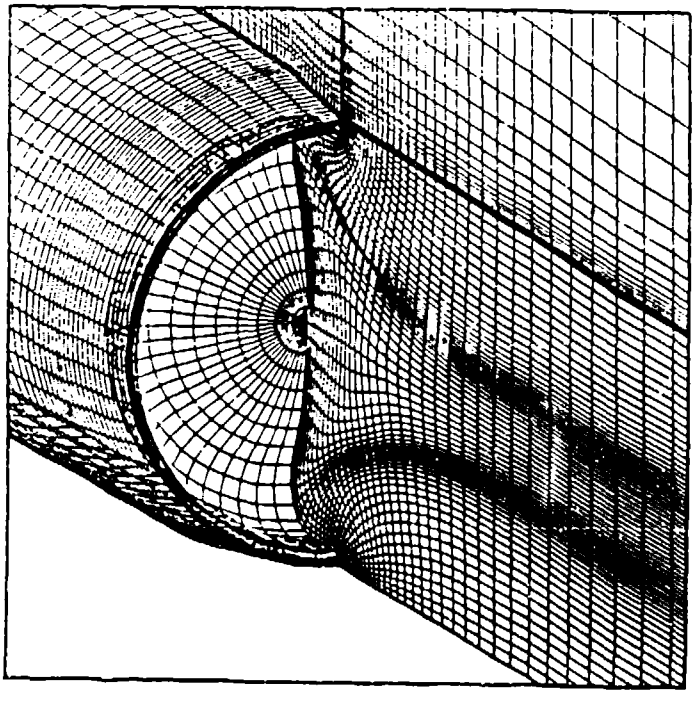

Figure 7: Base region grid for the dome base.

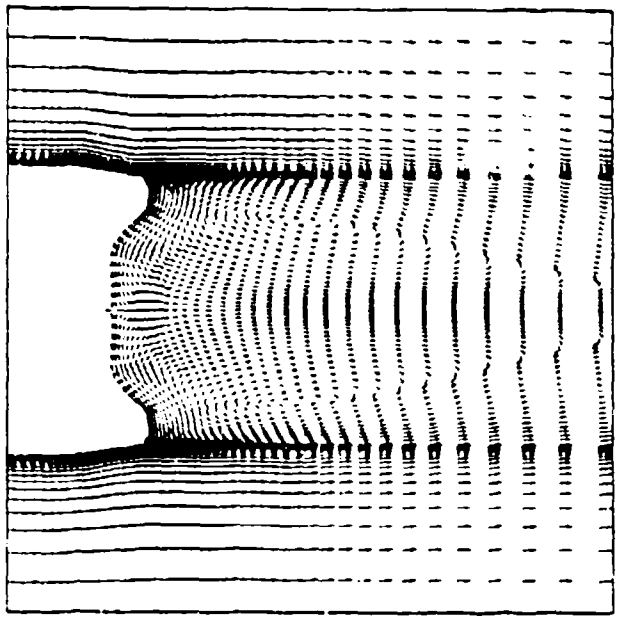

Figure 8. Velocity vectors in the base region, M_∞=0.98, $\alpha = 0.0^0$, (standard base)

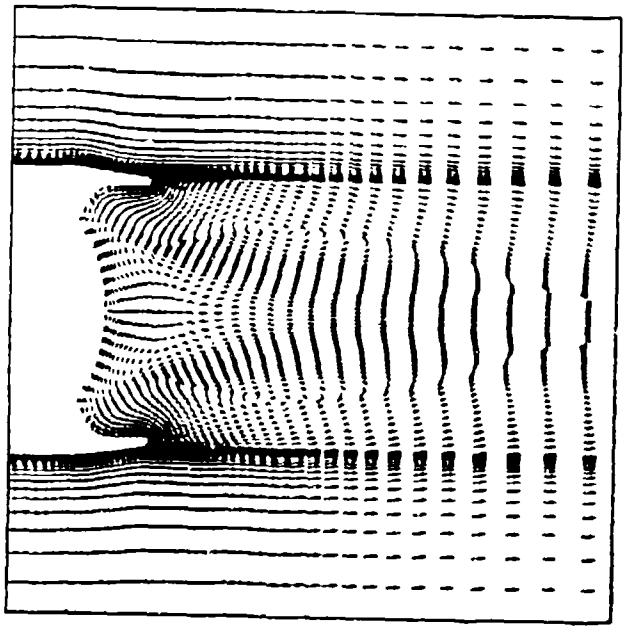

Figure 9. Velocity vectors in the base region, M_∞=0.98, $\alpha = 0.0^0$, (dome base).

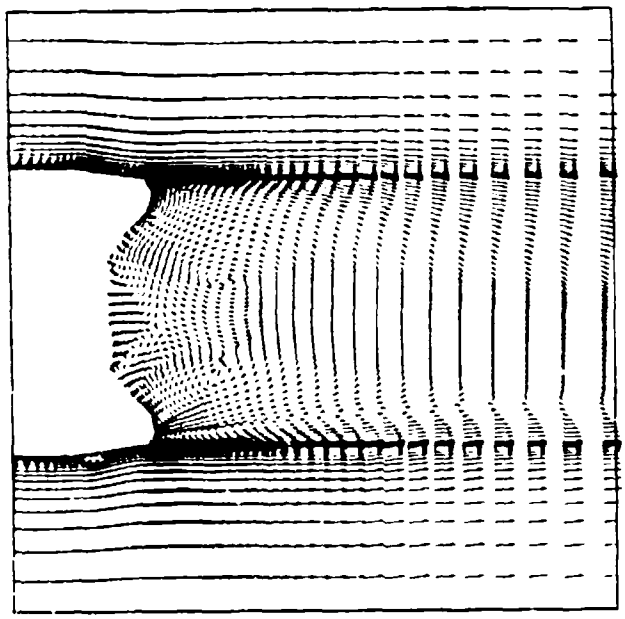

Figure 10 Velocity vectors in the base region, M_∞=0.98, α = 4.0^0, (standard base).

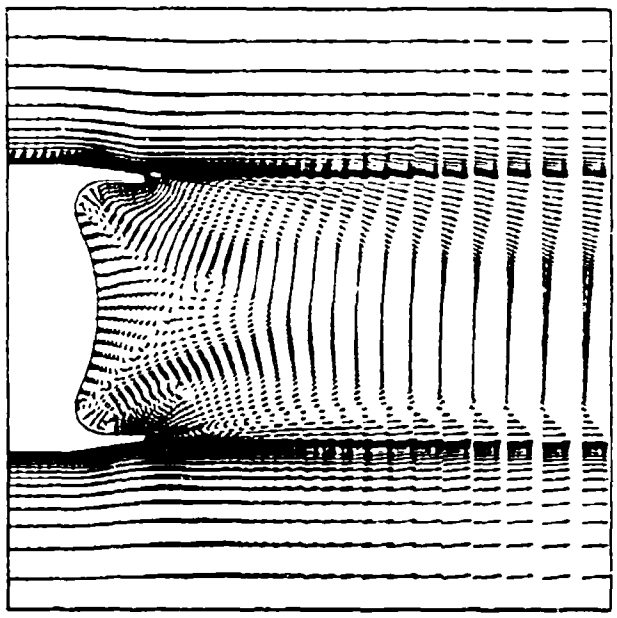

Figure 11: Velocity vectors in the base region, M_∞=0.98, α = 4.0^0, (dome base).

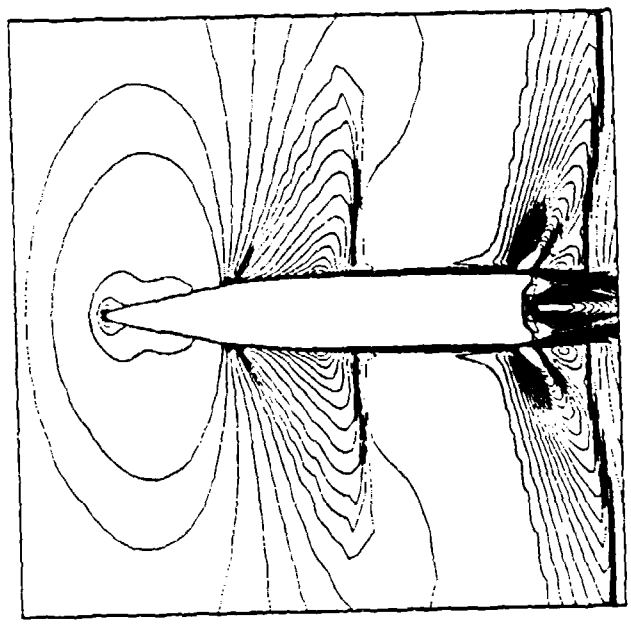

Figure 12. Mach number contours, M_∞=0.98, $\alpha = 0.0^0$, (standard base).

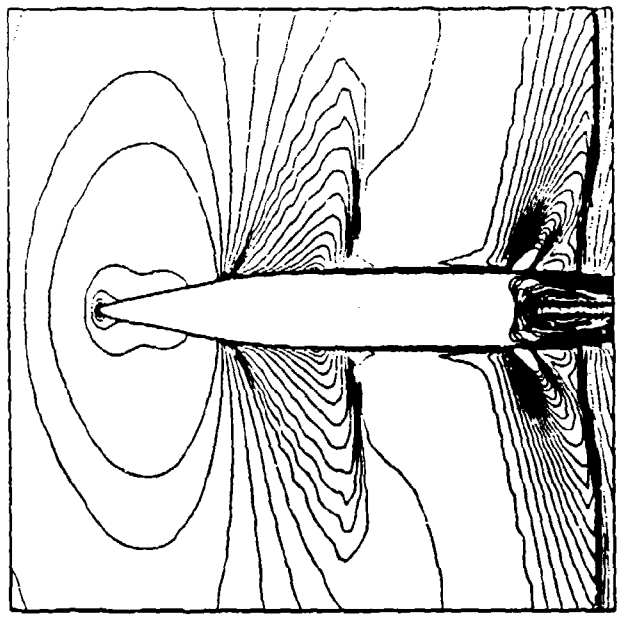

Figure 13: Mach number contours, M_∞=0.98, $\alpha = 0.0^0$, (dome base).

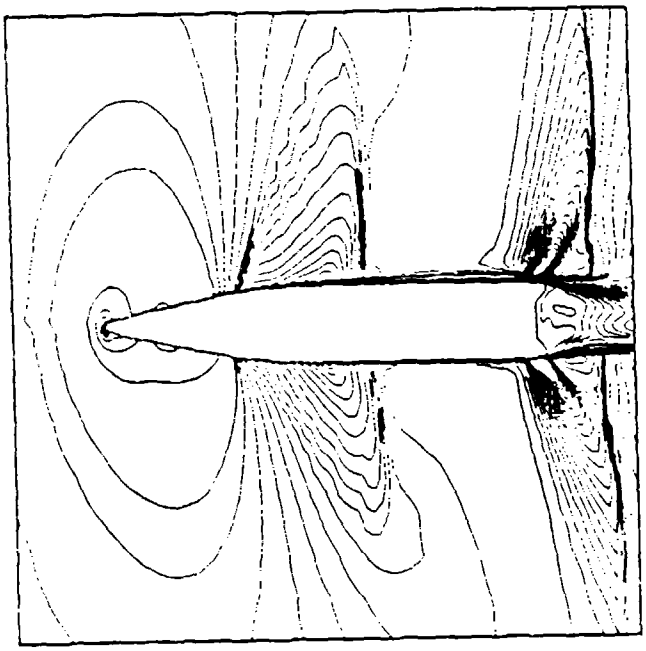

Figure 14: Mach number contours, M_∞=0.98, α = 4.0°, (standard base).

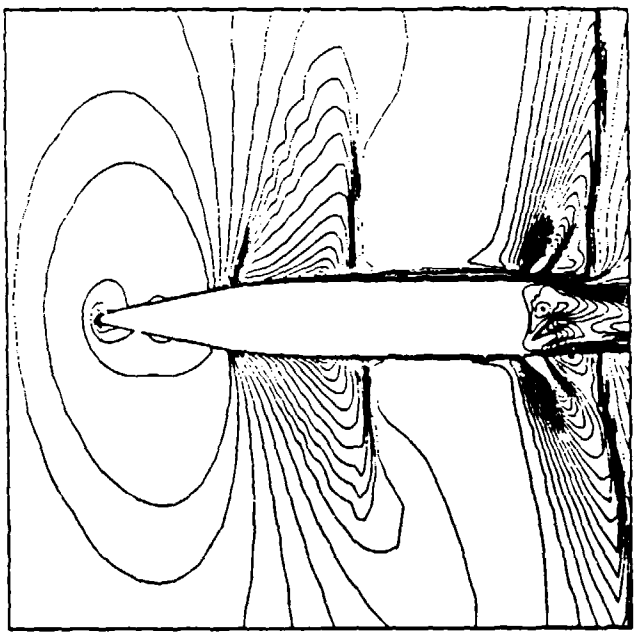

Figure 15: Mach number contours, M_∞=0.98, α = 4.0°, (dome base).

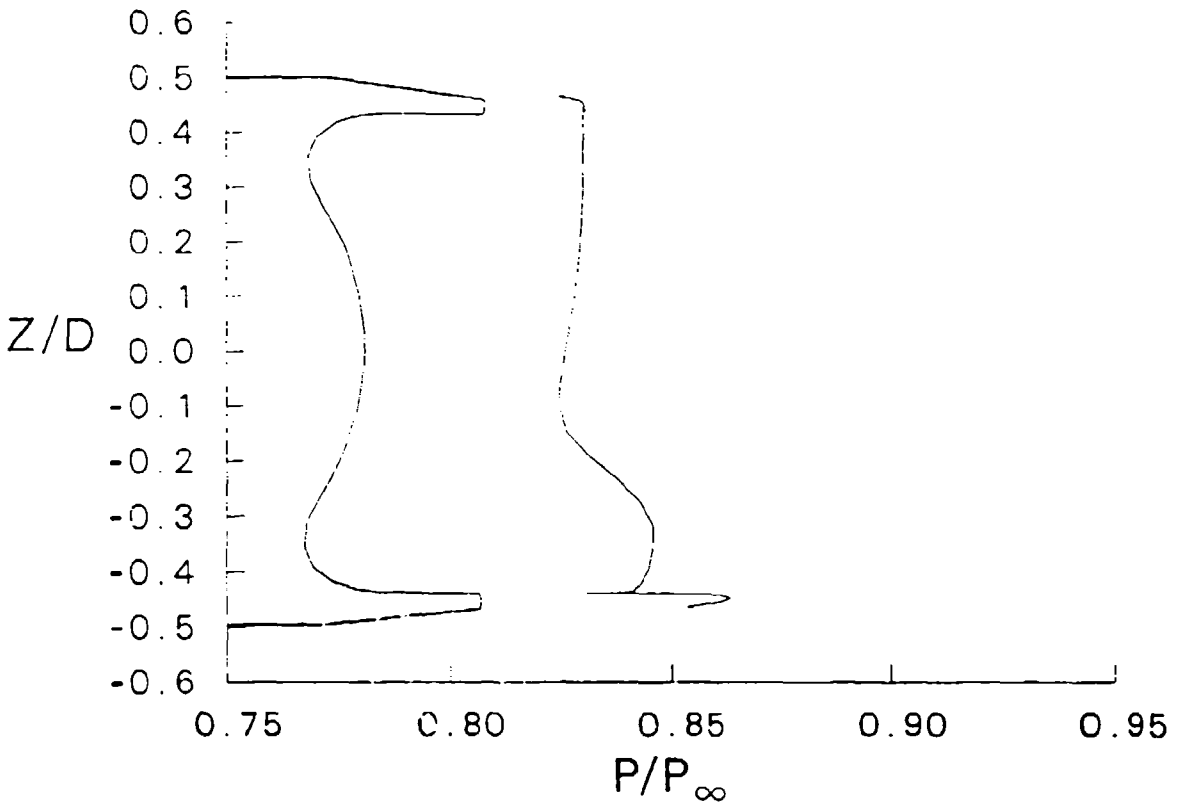

Figure 16. Base pressure distribution for the dome base,M_∞=1.1, $\alpha = 4.0^0$.

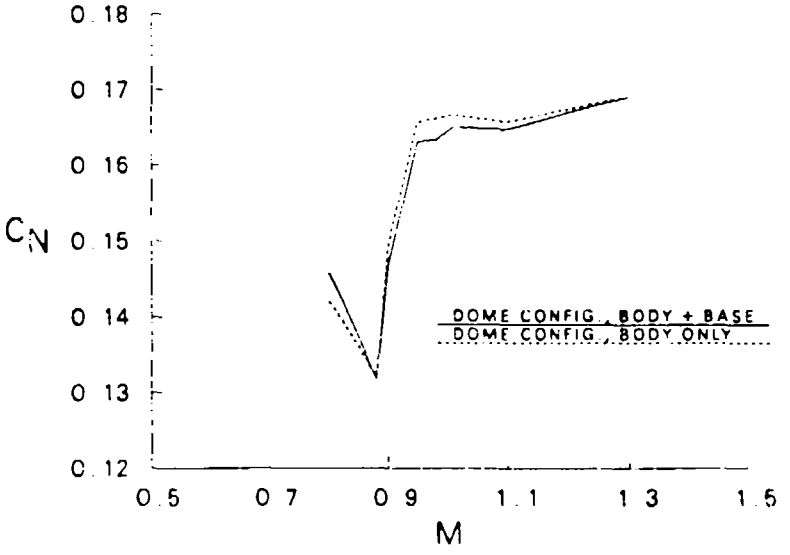

Figure 17. Normal force coefficient,C_N vs Mach number, $\alpha = 4.0^0$, (dome base).

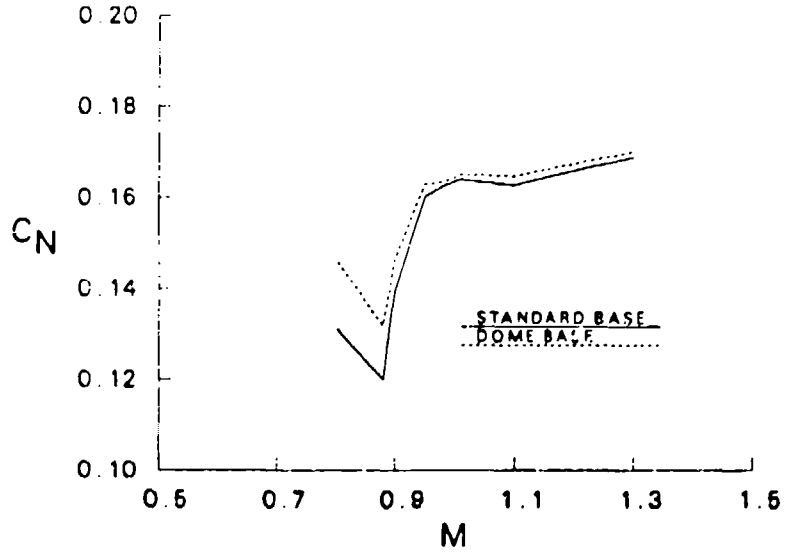

Figure 18. Normal force coefficient,C_N vs Mach number, $\alpha = 4.0^0$, (standard base and dome base).

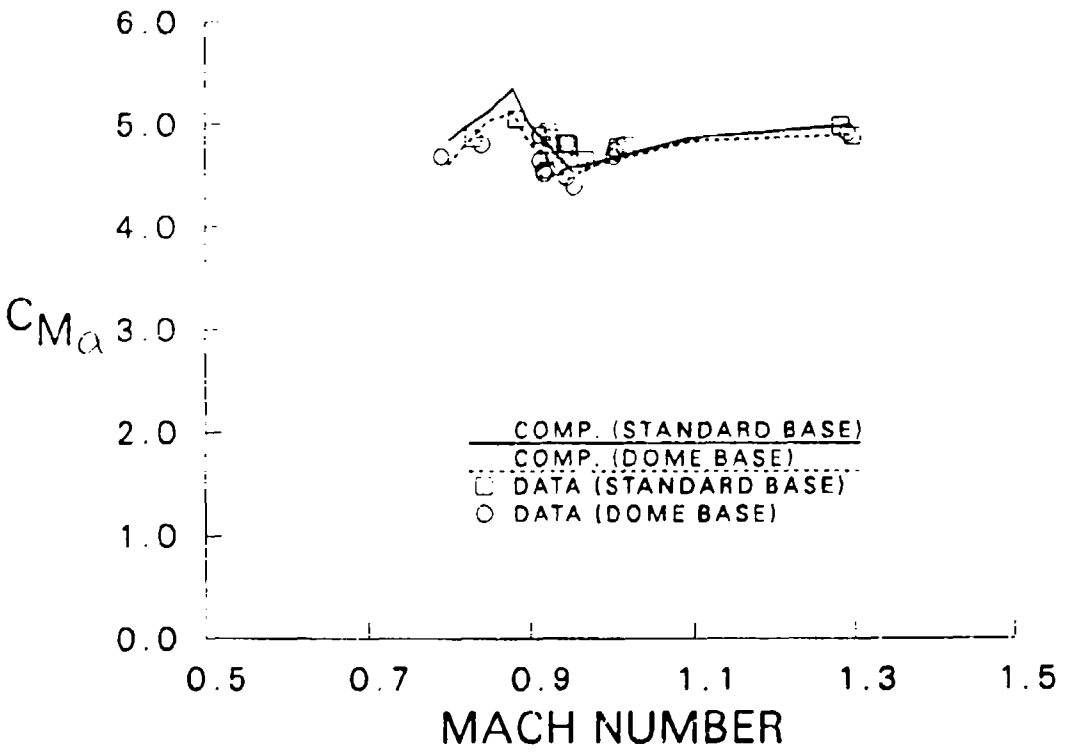

Figure 19. Pitching moment coefficient, C_{m_α} vs Mach number (standard base and dome base).

References

1. Sahu, J., Nietubicz, C.J. and Steger, J.L., "Navier-Stokes Computations of Projectile Base Flow with and without Base Injection," ARBRL-TR-02532, U.S. Army Ballistic Research Laboratory, Aberdeen Proving Ground, Maryland, November 1983. (AD A125738) (also see AIAA Journal, Vol. 23, No. 9, September 1985, pp. 1348-1355).

2. Sahu, J., "Computations of Supersonic Flow over a Missile Afterbody Containing an Exhaust Jet," AIAA Journal of Spacecraft and Rockets, Vol. 24, No. 5, September-October 1987, pp. 403-410.

3. Sahu, J., "Three Dimensional Base Flow Calculation for a Projectile at Transonic Velocity," BRL-MR-3610, U.S. Army Ballistic Research Laboratory, Aberdeen Proving Ground, Maryland, September 1987. (AD A184171)

4. D'Amico, W.P., Hepner, D.J., Clay, W.H., Davis, B.S., and Kendall, T.M., "Aeroballistic Testing of the M825 Projectile: Phase V. Dome Steel Base Product Improvement," BRL-MR-3554, U.S. Army Ballistic Research Laboratory, Aberdeen Proving Ground, Maryland, December 1986. (AD B115796)

5. Sahu, J., Nietubicz, C.J. and Heavey, K.R., "Computational Study of the M825 Projectile with Standard and Dome Bases," U.S. Army Ballistic Research Laboratory, BRL-MR-3662, Aberdeen Proving Ground, Maryland, March 1988. (AD A196206)

6. Pulliam, T.H. and Steger, J.L., "On Implicit Finite-Difference Simulations of Three-Dimensional Flow," AIAA Journal, Vol. 18, No. 2, February 1982, pp. 159-167.

7. Baldwin B.S. and Lomax, H., "Thin Layer Approximation and Algebraic Model for Separated Turbulent Flows," AIAA Paper No. 78-257, January 1978.

8. Sahu, J. and Steger, J.L., "Numerical Simulation of Three Dimensional Transonic Flows," BRL-TR-2903 U.S. Army Ballistic Research Laboratory, Aberdeen Proving Ground, Maryland, March 1988. (AD A194687) (also see AIAA Paper No. 87-2293, Atmospheric Flight Mechanics Conference, Monterey, California, August 1987).

9. Sahu, J., "Numerical Computations of Transonic Critical Aerodynamic Behavior," BRL-TR-2962, U.S. Army Ballistic Research Laboratory, Aberdeen Proving Ground, Maryland, December 1988. (AD A202412) (also see Paper No. 88-4038-CP, AIAA/ASME/SIAM/APS 1st National Fluid Dynamics Congress, Cincinnati, Ohio, July 1988).

10. Nietubicz, C.J., Heavey, K.R. and Steger, J.L., "Grid Generation Technique for Projectile Configurations," ARO Report 82-3, Proceedings of the 1982 Army Numerical Analysis and Computers Conference, August 1982.

INTENTIONALLY LEFT BLANK.

LIST OF SYMBOLS

a	speed of sound
c_p	specific heat at constant pressure
C_p	pressure coefficient
D	projectile diameter
e	total energy per unit volume
$\hat{F}, \hat{G}, \hat{H}$	flux vectors in transformed coordinates
J	jacobian
M	Mach number
Pr	Prandtl number
Pr_t	turbulent Prandtl number
$\hat{q}$	vector of dependent variables
R	body radius
$\hat{S}$	vector containing viscous terms
t	time
T	temperature
u,v,w	axial, circumferential, and normal velocity components of the Navier-Stokes equations
U,V,W	Contravariant velocities of the transformed Navier-Stokes equations
x,y..	physical Cartesian coordinates

Greek Symbols

α	Angle of attack
γ	ratio of specific heats
κ	molecular and turbulent thermal conductivity
μ	molecular and turbulent viscosity
ξ, η, ζ	transformed coordinates
ρ	density
ϕ	circumferential angle

Subscripts

∞	free stream conditions

Intentionally left blank.

No of Copies	Organization
1	Office of the Secretary of Defense OUSD(A) Director, Live Fire Testing ATTN: James F. O'Bryon Washington, DC 20301-3110
2	Administrator Defense Technical Info Center ATTN: DTIC-DDA Cameron Station Alexandria, VA 22304-6145
1	HQDA (SARD-TR) WASH DC 20310-0001
1	Commander US Army Materiel Command ATTN: AMCDRA-ST 5001 Eisenhower Avenue Alexandria, VA 22333-0001
1	Commander US Army Laboratory Command ATTN: AMSLC-DL Adelphi, MD 20783-1145
2	Commander US Army, ARDEC ATTN: SMCAR-IMI-I Picatinny Arsenal, NJ 07806-5000
2	Commander US Army, ARDEC ATTN: SMCAR-TDC Picatinny Arsenal, NJ 07806-5000
1	Director Benet Weapons Laboratory US Army, ARDEC ATTN: SMCAR-CCB-TL Watervliet, NY 12189-4050
1	Commander US Army Armament, Munitions and Chemical Command ATTN: SMCAR-ESP-L Rock Island, IL 61299-5000
1	Commander US Army Aviation Systems Command ATTN: AMSAV-DACL 4300 Goodfellow Blvd. St. Louis, MO 63120-1798

No of Copies	Organization
1	Director US Army Aviation Research and Technology Activity ATTN: SAVRT-R (Library) M/S 219-3 Ames Research Center Moffett Field, CA 94035-1000
1	Commander US Army Missile Command ATTN: AMSMI-RD-CS-R (DOC) Redstone Arsenal, AL 35898-5010
1	Commander US Army Tank-Automotive Command ATTN: AMSTA-TSL (Technical Library) Warren, MI 48397-5000
1	Director US Army TRADOC Analysis Command ATTN: ATAA-SL White Sands Missile Range, NM 88002-5502
(Class. only) 1	Commandant US Army Infantry School ATTN: ATSH-CD (Security Mgr.) Fort Benning, GA 31905-5660
(Unclass. only) 1	Commandant US Army Infantry School ATTN: ATSH-CD-CSO-OR Fort Benning, GA 31905-5660
1	Air Force Armament Laboratory ATTN: AFATL/DLODL Eglin AFB, FL 32542-5000
	Aberdeen Proving Ground
2	Dir, USAMSAA ATTN: AMXSY-D AMXSY-MP, H. Cohen
1	Cdr, USATECOM ATTN: AMSTE-TD
3	Cdr, CRDEC, AMCCOM ATTN: SMCCR-RSP-A SMCCR-MU SMCCR-MSI
1	Dir, VLAMO ATTN: AMSLC-VL-D

No. of Copies	Organization
3	Commander Naval Surface Warfare Center ATTN: Code R44, F. Priolo A. Wardlaw K24, B402-12, W. Yanta White Oak Laboratory Silver Spring, MD 20903-5000
2	Director NASA Langley Research Center ATTN: Technical Library Dr. M.J. Hemsch Langley Station Hampton, VA 23665
5	Director NASA Ames Research Center ATTN: MS-227-8, L. Schiff MS-258-1, T. Holst D. Chaussee M. Rai MS-258-3, P. Kutler Moffett Field, CA 94035
3	Commander US Army, ARDEC ATTN: SMCAR-AET-A, R. Kline H. Hudgins J. Grau Picatinny Arsenal, NJ 07806-5000
1	Commander Naval Surface Warfare Center ATTN: Dr. F. Moore Dahlgren, VA 22448
1	Air Force Armament Laboratory ATTN: AFATL/FXA, Stephen C. Korn Eglin AFB, FL 32542-5434

No. of Copies	Organization
1	USAF Wright Aeronautical Laboratories ATTN: AFWAL/FIMG, Dr. J. Shang WPAFB, OH 45433-6553
1	Massachusetts Institute of Technology ATTN: Technical Library 77 Massachusetts Avenue Cambridge, MA 02139
1	AEDC Calspan Field Service ATTN: MS 600, Dr. John Benek Tullahoma, TN 37389
1	Virignia Polytechnic Institute and State University Department of Aerospace and Ocean Engineering ATTN: Dr. Clark H. Lewis Blacksburg, VA 24061
2	University of California, Davis Department of Mechanical Engineering ATTN: Prof. H.A. Dwyer Prof. J.L. Steger Davis, CA 95616
1	Pennsylvania State University Department of Aerospace Engineering ATTN: Dr. G.S. Dulikravich University Park, PA 16802
1	University of Illinois at Urbana Champaign Department of Mechanical and Industrial Engineering ATTN: Dr. T.L. Addy Urbana, IL 61801
1	University of Maryland Department of Aerospace Engineering ATTN: Dr. J.D. Anderson, Jr. College Park, MD 20742

No. of Copies	Organization
1	University of Notre Dame Department of Aeronautical and Mechanical Engineering ATTN: Prof. T.J. Mueller Notre Dame, IN 46556
1	University of Texas Department of Aerospace Engineering and Engineering Mechanics ATTN: Dr. D.S. Dolling Austin, TX 78712-1055
2	Director Sandia National Laboratories ATTN: Dr. W.L. Oberkampf Dr. F. Blottner Division 1556 P.O. Box 5800 Albuquerque, NM 87185
2	University of Cincinnati Department of Aerospace Engineering ATTN: Prof. Stanley Rubin Prof. K.N. Ghia Mail Location 70 Cincinnati, OH 45221
1	Pennsylvania State University Department of Mechanical Engineering ATTN: Dr. Kenneth Kuo University Park, PA 16802
1	Florida Atlantic University Department of Mechanical Engineering ATTN: Dr. W.L. Chow Boca Raton, FL 33431
1	Georgia Institute of Technology School of Aerospace Engineering ATTN: Dr. Warren C. Strahle Atlanta, GA 30332
1	Scientific Research Associates ATTN: Dr. Howard Gibeling 50 Nye Road P.O. Box 1058 Glastonbury, CT 06033

INTENTIONALLY LEFT BLANK.

USER EVALUATION SHEET/CHANGE OF ADDRESS

This Laboratory undertakes a continuing effort to improve the quality of the reports it publishes. Your comments/answers to the items/questions below will aid us in our efforts.

1. BRL Report Number BRL-TR-3150 Date of Report SEPTEMBER 1990

2. Date Report Received _____

3. Does this report satisfy a need? (Comment on purpose, related project, or other area of interest for which the report will be used.) _____

4. Specifically, how is the report being used? (Information source, design data, procedure, source of ideas, etc.) _____

5. Has the information in this report led to any quantitative savings as far as man-hours or dollars saved, operating costs avoided, or efficiencies achieved, etc? If so, please elaborate. _____

6. General Comments. What do you think should be changed to improve future reports? (Indicate changes to organization, technical content, format, etc.) _____

CURRENT ADDRESS

Name

Organization

Address

City, State, Zip Code

7. If indicating a Change of Address or Address Correction, please provide the New or Correct Address in Block 6 above and the Old or Incorrect address below.

OLD ADDRESS

Name

Organization

Address

City, State, Zip Code

(Remove this sheet, fold as indicated, staple or tape closed, and mail.)